




The Halo Spin Transition As a Probe of Dark Energy

Jounghun Lee¹  and Noam I Libeskind^{2,3}¹Department of Physics and Astronomy, Seoul National University, Seoul 08826, Republic of Korea; jounghun@astro.snu.ac.kr²Leibniz-Institut für Astrophysik Potsdam (AIP), An der Sternwarte 16, D-14482 Potsdam, Germany; noam@aip.cn.kr³University of Lyon, UCB Lyon-1/CNRS/IN2P3, IPN Lyon, France

Received 2020 August 5; revised 2020 August 23; accepted 2020 August 25; published 2020 October 8

Abstract

We present numerical evidence supporting the claim that the mass-dependent transitions of the halo spin orientations from the intermediate to the minor principal directions of the local tidal fields can in principle be useful discriminators of dark energy models. We first define a *spin transition zone* as the mass range of the halos, Δm_i , for which the intrinsic spin alignments with the minor tidal principal directions become as strong as that with the intermediate principal directions. Then, utilizing the halo samples from the DEUS simulations performed separately for the WMAP7 Λ CDM, phantom dark energy, and quintessence models, we investigate if and how the three different dark energy models differ in Δm_i . It is shown that the differences in Δm_i among the three dark energy models are significant enough to discriminate the models from one another and robust against the variations of the smoothing scale of the tidal field and redshift. Noting that a narrower spin transition zone is more powerful as a probe of dark energy, we also show that the spin transition zones become narrower at higher redshifts in the filamentary environments and, for the case of the tidal fields, smoothed on smaller scales. Our result is consistent with the scenario that Δm_i is mainly determined by how fast the nonlinear evolution of the tidal field proceeds, which in turn sensitively depends on the background cosmology.

Unified Astronomy Thesaurus concepts: [Large-scale structure of the universe \(902\)](#); [Cosmological models \(337\)](#)

1. Introduction

Ever since the best-fit theoretical curves to the observed luminosity–distance relations of the SN Ia were found to be obtained from the Friedmann equations with nonvanishing cosmological constant term Λ (Riess et al. 1998; Perlmutter et al. 1999), it has been widely accepted that the present universe is in an accelerating phase caused by the negative pressure of the dominant energy content Λ with equation of state $w = P_\Lambda/\rho_\Lambda = -1$. Backed up further by the observations of the cosmic microwave background (CMB) temperature power spectrum and the large-scale structures (e.g., Tegmark et al. 2004; Komatsu et al. 2011, and references therein), what has been established as a standard model of cosmology for the past two decades is an inflationary flat universe containing the dominant Λ and nonbaryonic cold dark matter (CDM), being often dubbed the Λ CDM cosmology.

The solidity of the Λ CDM cosmology as a physical model has been known to be overcast by two conceptual problems associated with Λ . First, its value inferred from the SN Ia observation is too low to be explicable by any fundamental physics. Second, it requires unnaturally fine-tuned initial conditions to explain the observed ratio of the matter to Λ density parameter being an order of unity, $\Omega_m/\Omega_\Lambda \sim 1$, at the present epoch (Carroll 2001, 2006). Nonetheless, the simplicity and effectiveness of the Λ CDM cosmology in explaining the large-scale features of the universe at a quantitative level has justified connivance of the community at these profound problems (Springel et al. 2006).

The latest observational data measured with unprecedentedly high precision and analyzed with the cutting-edge statistical techniques, however, have signaled a rupture between the early and the late universes described by the Λ CDM model. The most notorious example of this rupture is the value of the Hubble constant, H_0 , obtained from the observations of the local Cepheids, which turned out to be in 4.4σ tension with its

best-fit value from the latest CMB analysis (Riess et al. 2019; Planck Collaboration et al. 2020). Another example is the amplitude of the linear density power spectrum, σ_8 and density parameter, Ω_m , whose best-fit values from the cosmic shear surveys showed mismatches with the central values from the latest CMB analysis under the assumption of a Λ CDM universe (Abbott et al. 2018; Hikage et al. 2019). Although various attempts have been made to reconcile the near-field measurements with the CMB best fits (e.g., Agrawal et al. 2019; Poulin et al. 2019; Kreisch et al. 2020), none of them have so far been fully satisfactory.

Being progressively perceived as a cardinal drawback of the Λ CDM model rather than being casually ascribed to some unidentified systematics, the aforementioned rupture drew attention to the importance and necessity of developing competitive near-field probes to distinguish between the viable alternative DE and the Λ CDM models, which equally satisfy the CMB constraints. What has been sought after as an optimal near-field probe is the one that describes the small-scale features of the universe in the deeply nonlinear regime and concurrently possesses a sensitive dependence on the background cosmology.

Very recently, Lee et al. (2020) suggested a new near-field diagnostics based on the mass-dependent transition of the halo spins, which refers to the numerically and observationally detected phenomenon that while the high-mass halos have their spins preferentially aligned with the directions perpendicular to the minor principal axes of the local tidal fields, the low-mass ones prefer the directions parallel to them in their spin orientations (e.g., Aragón-Calvo et al. 2007; Hahn et al. 2007a, 2010; Paz et al. 2008; Codis et al. 2012, 2015a, 2015b, 2018; Libeskind et al. 2013; Tempel & Libeskind 2013; Tempel et al. 2013; Trowland et al. 2013; Aragón-Calvo & Yang 2014; Dubois et al. 2014; Forero-Romero et al. 2014; Welker et al. 2014, 2020; Laigle et al. 2015; Pahwa et al. 2016;

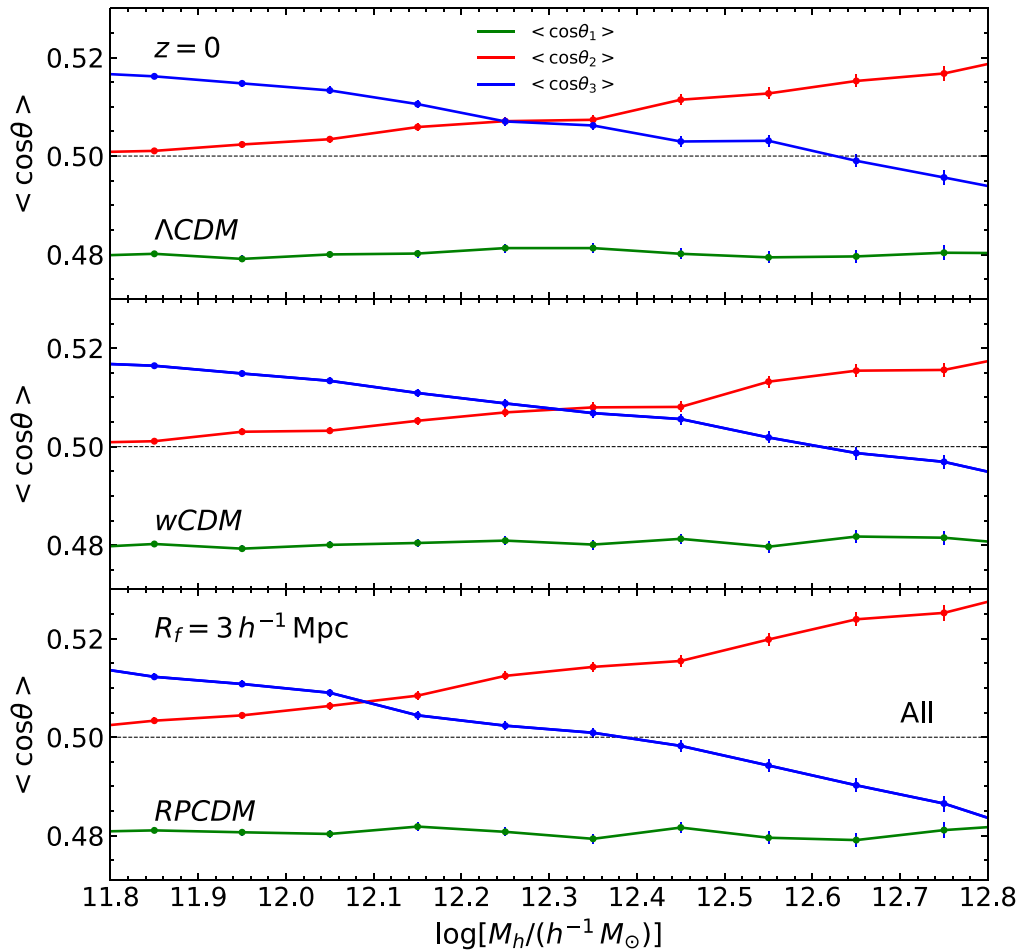


Figure 1. Ensemble average of the cosines of the angles between the unit spin vectors of DM halos and three principal directions of the local tidal fields at $z = 0$ as a function of the halo mass for three different dark energy models.

Hirv et al. 2017; Ganeshiah Veena et al. 2018, 2019; Wang et al. 2018; Wang & Kang 2018; Blue Bird et al. 2019; Krolewski et al. 2019; Lee 2019; Kraljic et al. 2020). What Lee et al. (2020) newly found was that the critical mass at which the transition of the halo spin orientations occurs (transition mass of the halo spins) varies sensitively with the total neutrino mass, regardless of the smoothing scale of the tidal field.

In light of Lee et al. (2020), we set off here to numerically explore if the transition mass of the halo spins can be used as a probe of DE with the help of N -body simulations. The contents of this paper can be outlined as follows. In Section 2.1 we describe a data set from N -body simulations for three different dark energy models and present a routine with which the mass-dependent transitions of the halo spins are determined. In Section 2.2, we present numerical evidence for the usefulness of the halo spin transitions as a discriminator of dark energy models. In Section 2.3, we describe how the sensitivity of the halo spin transitions as a probe of dark energy varies with the cosmic web type. In Section 3, we summarize the main results and discuss their implications.

2. Effect of DE on the Transition Mass of the Halo Spins

2.1. Data and Routine

For the current study, we consider three different DE models, namely, a flat Λ CDM model with equation of state $w = -1$, a phantom DE model with negative constant equation of state

Table 1
Initial Conditions and the Particle Mass Resolution

Model	Ω_m	h	σ_8	w_0	w_a	m_p ($10^9 h^{-1} M_\odot$)
Λ CDM	0.257	0.72	0.80	-1.0	0.0	2.3
w CDM	0.275	0.72	0.852	-1.2	0.0	2.4
RPCDM	0.230	0.72	-0.66	-0.87	0.08	2.0

$w < -1$, and a quintessence model with time varying equation of state $-1 < w(t) < -2/3$, simulated by the Dark Energy Universe Simulation (DEUS) project in a periodic box of comoving volume $648^3 h^{-3} \text{Mpc}^3$ with 2048^3 DM particles (Rasera et al. 2010; Alimi et al. 2012; Bouillot et al. 2015). For the flat Λ CDM model, the six key cosmological parameters were set at the central values determined by the Wilkinson Microwave Anisotropy Probe Seven Year data (WMAP7) (Spergel et al. 2007; Komatsu et al. 2011). For the other two DE models, the values of the seven cosmological parameters (the six key parameters + w) were chosen to satisfy the same WMAP7 constraints. Table 1 lists the values of the matter density parameter, Ω_m , linear power spectrum amplitude on the scale of $8 h^{-1} \text{Mpc}$, σ_8 , dimensionless Hubble parameter, h , dark energy equation of state, $w \equiv w_0 + w_a(1 - a)$ with scale factor $a(t)$ (Linder 2003), and mass of individual DM particles,

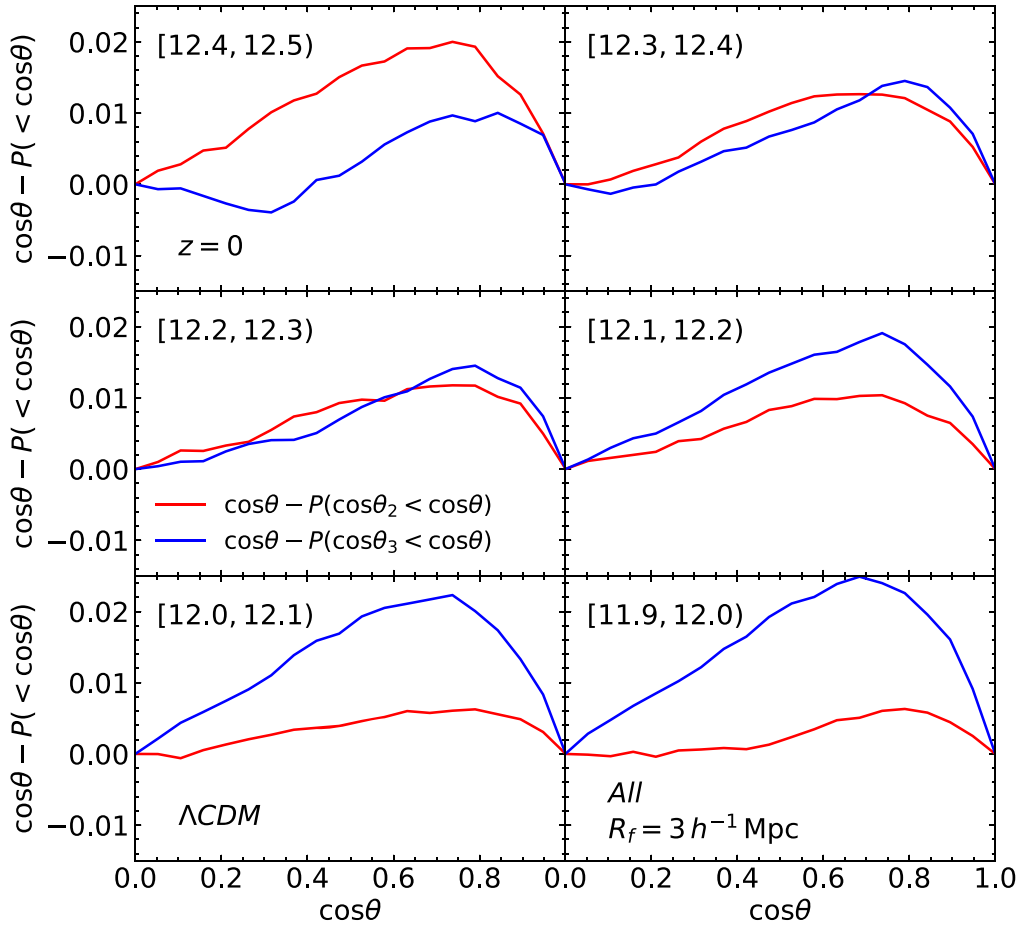


Figure 2. Differences between $\cos \theta$ and the cumulative probability distribution $P(\cos \theta_i < \cos \theta)$ with $i \in \{2, 3\}$ at six different mass bins at $z = 0$ for the Λ CDM model.

m_p , for the three DE models. For a more detailed description of the DEUS, we refer the readers to Alimi et al. (2012) as well as the DEUS webpage.⁴

A phantom DE (w CDM) is characterized by its negative kinetic energy that exerts stronger repulsive force than Λ (Caldwell et al. 2003). Whereas, a quintessence model is characterized by the potential shape of a scalar field DE. For the DEUS, the Ratra–Peebles potential, whose shape is expressed as powers of linear combinations of the exponentials of the scalar field (Ratra & Peebles 1988), was specifically chosen. Although the distant-field diagnostics based on the linear observables like the CMB temperature spectra and SN Ia luminosity–distance relations cannot distinguish among the three models (Bouillot et al. 2015), an efficient near-field probe based on the nonlinear observables might be able to pull it off since the formation and evolution of the nonlinear structures proceed in a different way among them (e.g., see Alimi et al. 2010).

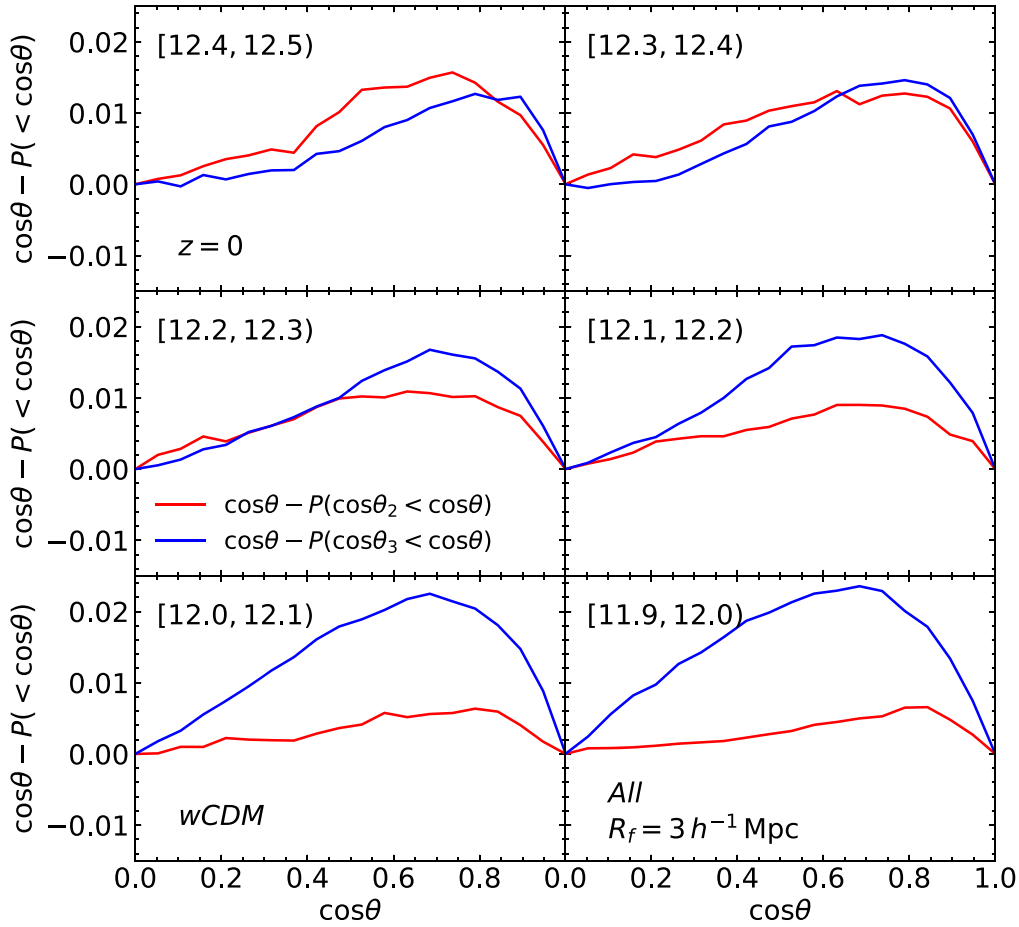
The halo catalog from the DEUS comprises the gravitationally bound objects identified at various redshifts by the Friends-of-Friends (FoF) halo finder with a linkage parameter of 0.2 (Roy et al. 2014) and provides information not only on the center of mass position, \mathbf{x} , and virial mass, M_h , of each object but also on the positions and velocities of its constituent DM particles, which allow us to compute its angular momentum

vector, $\mathbf{S} \equiv S\hat{\mathbf{S}}$. The well-resolved FoF objects in the mass range of $11.8 \leq \log[M_h / (h^{-1}M_\odot)] \leq 13$ at $z = 0$ are selected for a sample of the galactic halos to be used for the current analysis. The low-mass FoF objects with $\log[M_h / (h^{-1}M_\odot)] < 11.8$ are excluded from our analysis on the ground that the angular momentum vectors of the halos composed of less than 300 DM particles are likely to suffer from inaccuracy caused by the shot noise (Bett et al. 2007).

The routine we go through for the investigation of the DE dependence of the halo spin transitions is similar to that described in Lee et al. (2020), the summary of which is provided in the following.

1. Divide the simulation volume into 256^3 grids and create a density field, $\rho(\mathbf{x})$, on the grids by applying the cloud-in-cell method to the DM halo distributions from the DEUS. Calculate the dimensionless density contrast field, $\delta(\mathbf{x}) \equiv [\rho(\mathbf{x}) - \langle \rho \rangle] / \langle \rho \rangle$, where $\langle \rho \rangle$ is the spatial average of $\rho(\mathbf{x})$ taken over the 256^3 grids.
2. Evaluate the Fourier-space density contrast field, $\tilde{\delta}(\mathbf{k})$, by applying the fast-Fourier transformation method to $\delta(\mathbf{x})$, where $\mathbf{k} = (k\hat{\mathbf{k}})$ is the Fourier-space wavevector. Create a tidal shear field, $\mathbf{T}(\mathbf{x}) = [T_{ij}(\mathbf{x})]$, smoothed with a Gaussian filter on the scale of R_f via the inverse Fourier transformation of $\tilde{\delta}(\mathbf{k}) \exp(-k^2 R_f^2 / 2) \hat{\mathbf{k}}_i \hat{\mathbf{k}}_j$. At each grid, diagonalize $T_{ij}(\mathbf{x})$ to determine its three eigenvalues, $\{\lambda_1, \lambda_2, \lambda_3\}$ with $\lambda_1 \geq \lambda_2 \geq \lambda_3$, and corresponding

⁴ All data from the DEUS are publicly available at <http://www.deus-consortium.org/>.

Figure 3. Same as Figure 2 but for the w CDM model.

orthonormal eigenvectors, $\{\hat{p}_1, \hat{p}_2, \hat{p}_3\}$ as the major, intermediate, and minor principal directions.

- Find at which grid each selected halo is placed. Calculate three cosines of the angles at the grid, $\cos \theta_i = |\hat{S} \cdot \hat{p}_i|$ for $i \in \{1, 2, 3\}$. Divide the range of the logarithmic masses of the galactic halos, $m_h \equiv \log[M_h/(h^{-1}M_\odot)]$, into multiple differential intervals, $[m_h, m_h + dm_h]$ with $dm_h = 1$. Determine the probability densities, $p(\cos \theta_i)$, by counting the number, n_g , of the halos whose masses fall in each differential interval and take the ensemble averages as $\langle \cos \theta_i \rangle \equiv \int_0^1 p(\cos \theta_i) \cos \theta_i d \cos \theta_i$ at each differential interval. The error, $\sigma_{\langle \cos \theta_i \rangle}$, in the measurement of each ensemble average is calculated as the one standard deviation in the mean: $\sigma_{\langle \cos \theta_i \rangle}^2 \equiv [\int_0^1 p(\cos \theta_i) (\cos \theta_i - \langle \cos \theta_i \rangle)^2 d \cos \theta_i] / (n_g - 1)$.

2.2. Spin Transition Zone

Figure 1 plots $\langle \cos \theta_1 \rangle$ (blue line), $\langle \cos \theta_2 \rangle$ (red line), and $\langle \cos \theta_3 \rangle$ (green line) with one standard deviation errors at $z = 0$ as functions of m_h for the Λ CDM (top panel), w CDM (middle panel), and RPCDM (bottom panel) models. For this plot, the scale radius R_f of the Gaussian filter is set at $3 h^{-1} \text{ Mpc}$. In each panel, the horizontal black dotted line corresponds to the expected value of $\langle \cos \theta_i \rangle$ for the case that \hat{S} is randomly oriented with respect to \hat{p}_i . For all three models, we find that $\langle \cos \theta_2 \rangle$ ($\langle \cos \theta_3 \rangle$) is an increasing (decreasing) function of m_h

while $\langle \cos \theta_1 \rangle$ shows almost no variation, being negative constant in the whole range of $11.5 \leq m_h \leq 13$, and that the two functions, $\langle \cos \theta_2 \rangle$ and $\langle \cos \theta_3 \rangle$ intersect each other at a certain threshold mass, signaling the occurrence of the halo spin transition from the \hat{S} - \hat{p}_3 alignments from the \hat{S} - \hat{p}_2 alignments. The three models, however, differ in the rate at which $\langle \cos \theta_2 \rangle$ ($\langle \cos \theta_3 \rangle$) increases (decreases) with m_h as well as in the value of the threshold mass.

Instead of regarding the threshold mass at which $\langle \cos \theta_2 \rangle \sim \langle \cos \theta_3 \rangle$ as the transition mass of the halo spins, however, we adopt the more rigorous definition given by Lee et al. (2020), according to which the spin transition occurs in a differential mass interval where the null hypothesis of $p(\cos \theta_2) \sim p(\cos \theta_3)$ is rejected by the Kolmogorov–Smirnov (KS) test at a confidence level lower than 99.9%. For the KS test of the null hypothesis of $p(\cos \theta_2) \sim p(\cos \theta_3)$ at each m_h -interval, we evaluate two cumulative probability functions, $P(\cos \theta_2 < \cos \theta) \equiv \int_0^{\cos \theta} p(\cos \theta_2) d \cos \theta_2$ and $P(\cos \theta_3 < \cos \theta) \equiv \int_0^{\cos \theta} p(\cos \theta_3) d \cos \theta_3$.

Figure 2 compares $P(\cos \theta_2 < \cos \theta)$ (red line) with $P(\cos \theta_3 < \cos \theta)$ (blue line) at six different m_h -intervals, $12.4 \leq m_h < 12.5$ (top left panel), $12.3 \leq m_h < 12.4$ (top right panel), $12.2 \leq m_h < 12.3$ (middle left panel), $12.1 \leq m_h < 12.2$ (middle right panel), $12.0 \leq m_h < 12.1$ (bottom left panel), and $11.9 \leq m_h < 12.0$ (bottom right panel), for the Λ CDM case at $z = 0$. The same comparisons between the two cumulative distributions but for the w CDM and

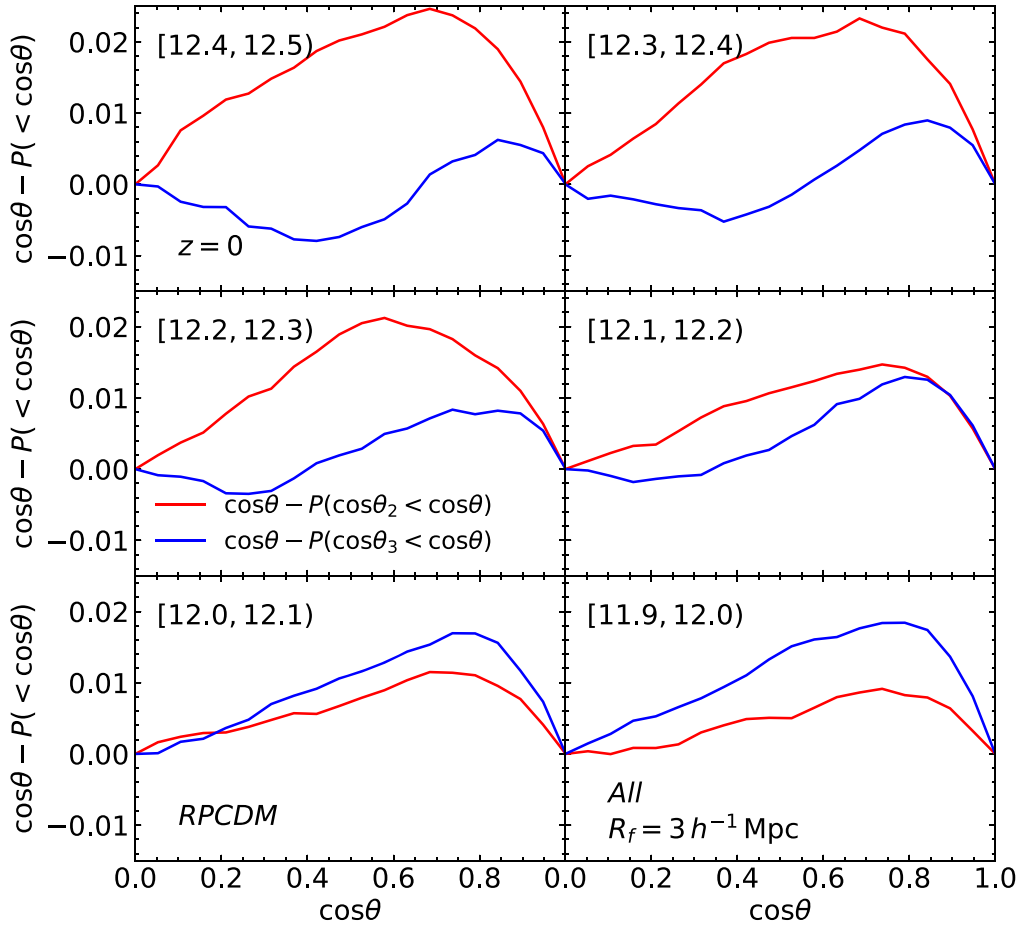


Figure 4. Same as Figure 2 but for the RPCDM model.

RPCDM cases are made in Figures 3 and 4, respectively. To show more clearly the differences between $P(\cos \theta_2 < \cos \theta)$ and $P(\cos \theta_3 < \cos \theta)$, we plot $\cos \theta - P(\cos \theta_i < \cos \theta)$ in lieu of $P(\cos \theta_i < \cos \theta)$ in Figures 2–4, as done in Lee et al. (2020).

In the differential interval of $12.4 \leq m_h < 12.5$, we find $P(\cos \theta_2 < \cos \theta) \sim P(\cos \theta_3 < \cos \theta)$ for the w CDM case but $P(\cos \theta_2 < \cos \theta) \approx P(\cos \theta_3 < \cos \theta)$ for the other two cases. In the differential interval of $12.3 \leq m_h < 12.4$, we find $P(\cos \theta_2 < \cos \theta) \sim P(\cos \theta_3 < \cos \theta)$ for the w CDM and Λ CDM cases, but $P(\cos \theta_2 < \cos \theta) \approx P(\cos \theta_3 < \cos \theta)$ for the RPCDM case. In the differential interval of $12.0 \leq m_h < 12.1$, we find $P(\cos \theta_2 < \cos \theta) \sim P(\cos \theta_3 < \cos \theta)$ for the RPCDM case, but $P(\cos \theta_2 < \cos \theta) \approx P(\cos \theta_3 < \cos \theta)$ for the w CDM and Λ CDM cases. These results clearly indicate that the three DE models differ in the mass intervals where $p(\cos \theta_2) \sim p(\cos \theta_3)$.

We compute the maximum distance, D_{\max} , between $P(\cos \theta_2 < \cos \theta)$ and $P(\cos \theta_3 < \cos \theta)$ at each m_h -interval and multiply it by the weighting factor $\sqrt{n_h/2}$, where n_h denotes the number of halos in each m_h -interval. Note that both D_{\max} and n_h are functions of m_h , i.e., $D_{\max} = D_{\max}(m_h)$ and $n_h = n_h(m_h)$. If this weighted maximum distance turns out to be lower (higher) than the critical value, 1.949, at a given m_h -interval, then the KS test rejects the null hypothesis of $p(\cos \theta_2) \sim p(\cos \theta_3)$ at the confidence level lower (higher) than 99.9%. Introducing a new concept, the *spin transition*

zone, Δm_t , defined as

$$\Delta m_t = \left\{ m_h \left| \sqrt{\frac{1}{2} n_h(m_h)} D_{\max}(m_h) < 1.949 \right. \right\}, \quad (1)$$

we take into account the fact that the halo spin transition does not occur sharply at a singular threshold mass scale but gradually proceeds in a finite mass range.

Figure 5 plots the weighted maximum distance, $\sqrt{n_h/2} D_{\max}$, between $P(\cos \theta_2 < \cos \theta)$ and $P(\cos \theta_3 < \cos \theta)$ as a function of m_h for the three models. In each panel, the horizontal black dashed line corresponds to the critical value, 1.949 for the 99.9% confidence level according to the KS test. As can be seen, the three DE models have significantly different spin transition zones: $\Delta m_t = \{m_h | 12.2 \leq m_h < 12.4\}$ (Λ CDM), $\Delta m_t = \{m_h | 12.2 \leq m_h < 12.5\}$ (w CDM), and $\Delta m_t = \{m_h | 12.0 \leq m_h < 12.1\}$ (RPCDM). The spin transition zone of the RPCDM model turns out to be most conspicuously different from those of the other two models, being biased toward the significantly lower mass section. Although the spin transition zone of the Λ CDM model is overlapped with that of the w CDM model, the two models can still be distinguished by the nonoverlapped m_h -interval, $12.4 \leq m_h \leq 12.5$, where the null hypothesis is rejected by the KS test at a confidence level higher than 99.9% for the Λ CDM case but not for the w CDM case. In other words, the halos with masses in the range of $12.4 \leq m_h \leq 12.5$ do not show a spin transition for the Λ CDM case, while they do for the w CDM case.

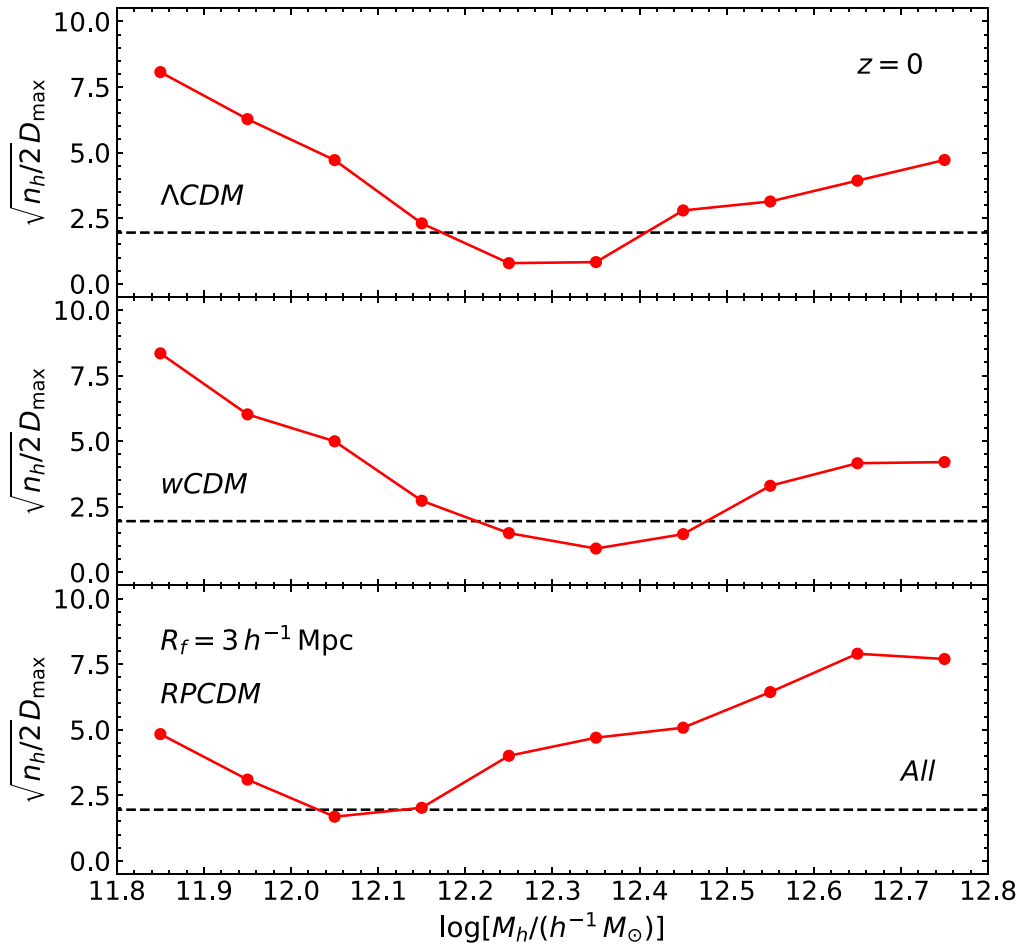


Figure 5. Maximum distances between $P(\cos \theta_2 < \cos \theta)$ and $P(\cos \theta_3 < \cos \theta)$ multiplied by $\sqrt{n_h/2}$ as a function of the halo mass at $z = 0$ for the three DE models.

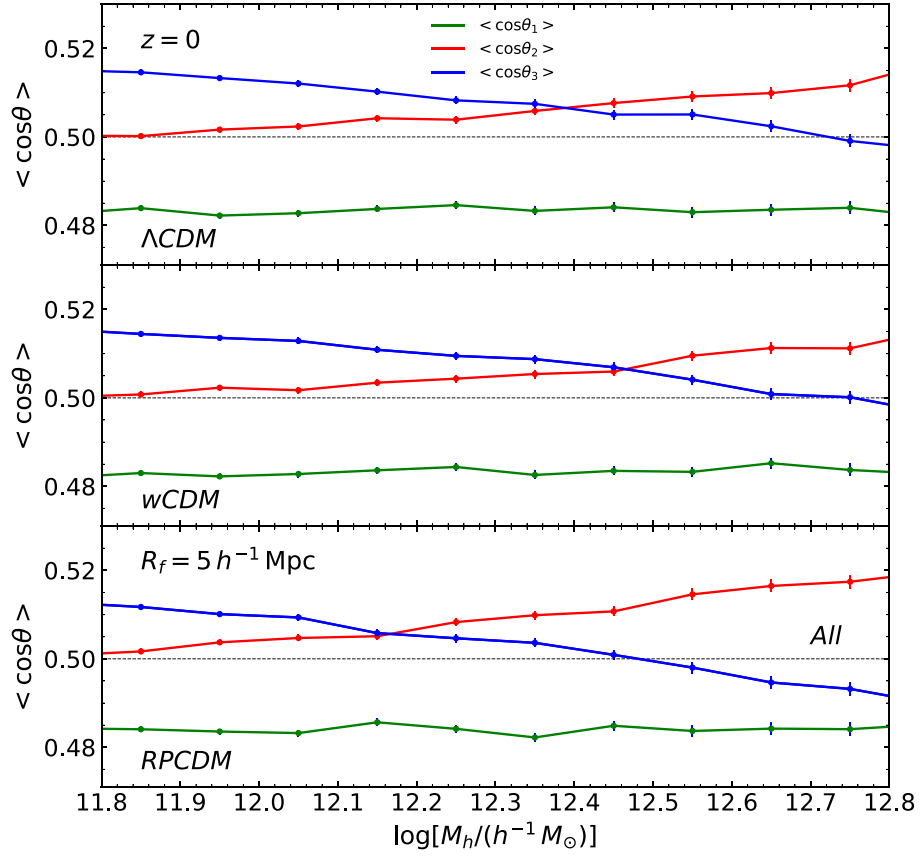
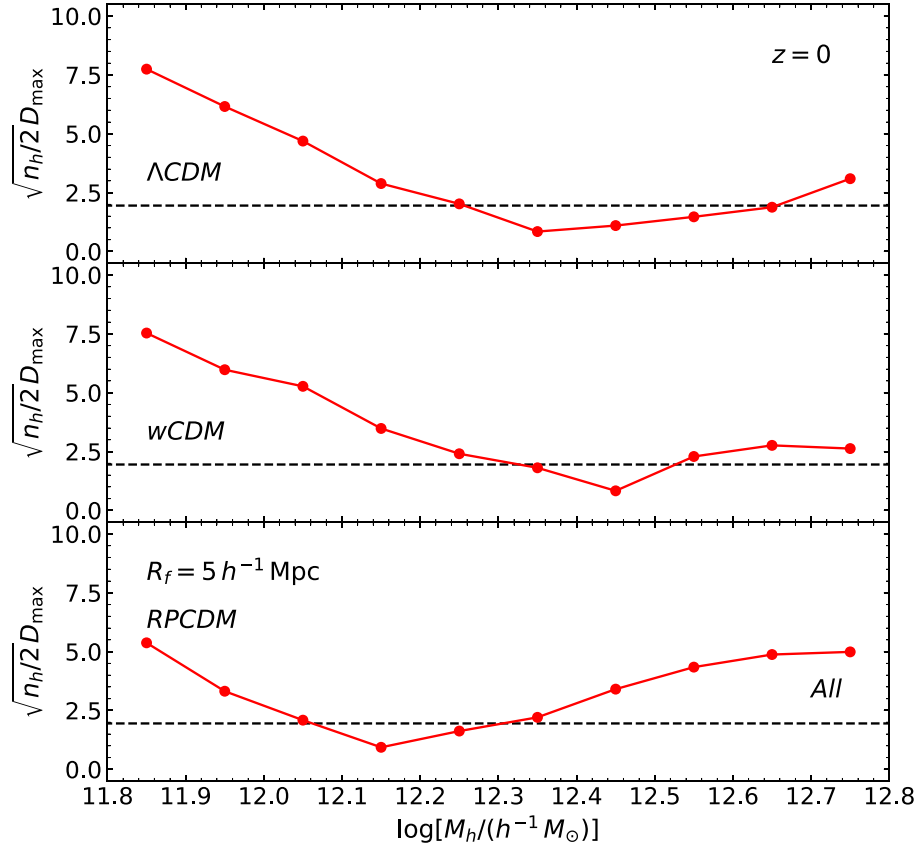
Smoothing the tidal shear field on a larger scale $R_f = 5 h^{-1} \text{ Mpc}$, we recalculate $\langle \cos \theta_i \rangle$ and $\sqrt{n_h/2} D_{\text{max}}$, which are depicted in Figures 6 and 7, respectively. As can be seen, the variation of R_f to $5 h^{-1} \text{ Mpc}$ does not weaken the DE dependence of Δm_t , although it has an effect of slightly widening Δm_t for all of the three models. We find $\Delta m_t = \{m_h | 12.3 \leq m_h < 12.6\}$ (ΛCDM), $\Delta m_t = \{m_h | 12.3 \leq m_h < 12.5\}$ ($w\text{CDM}$), and $\Delta m_t = \{m_h | 12.1 \leq m_h < 12.3\}$ (RPCDM). The RPCDM model can still be readily distinguished from the other two models by its spin transition zone in the lowest mass section. The ΛCDM and $w\text{CDM}$ models still significantly differ from each other in the nonoverlapped interval of $12.5 \leq m_h < 12.6$ where the null hypothesis of $p(\cos \theta_2) \sim p(\cos \theta_3)$ is rejected at the confidence level higher (lower) than 99.9% levels for the latter (former) model.

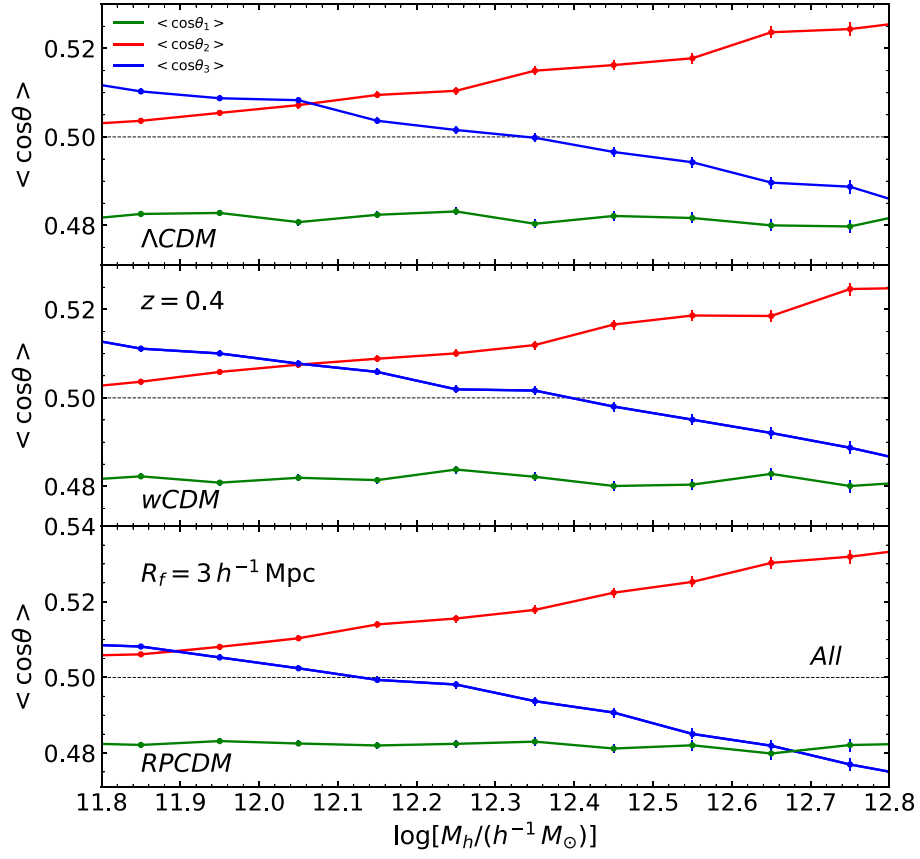
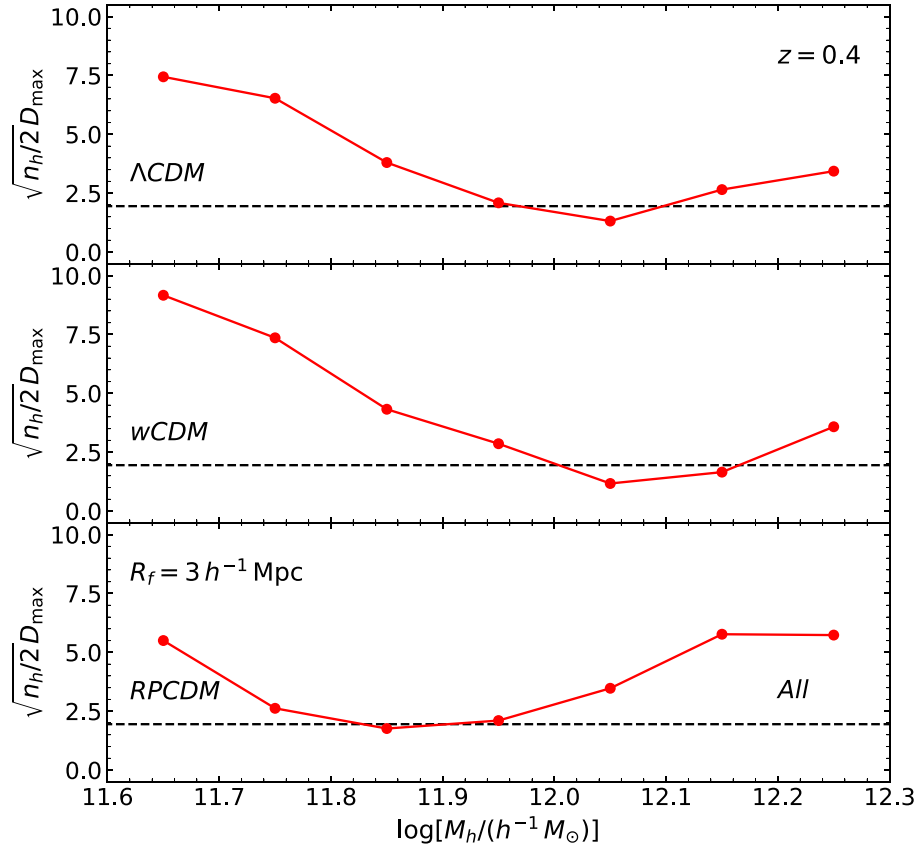
Using the halo catalog at $z = 0.4$ from the DEUS and resetting R_f at $3 h^{-1} \text{ Mpc}$, we go through the same routine to determine $\langle \cos \theta_i \rangle$ and $\sqrt{n_h/2} D_{\text{max}}$ at $z = 0.4$, which are depicted in Figures 8 and 9, respectively. As can be seen, at higher redshifts, the spin transition zones become narrower, showing considerable shifts toward the lower mass sections for all of the three models. The spin transition zones at $z = 0.4$ are found to be $\Delta m_t = \{m_h | 12.0 \leq m_h < 12.1\}$ (ΛCDM), $\Delta m_t = \{m_h | 12.0 \leq m_h < 12.2\}$ ($w\text{CDM}$), and $\Delta m_t = \{m_h | 11.8 \leq m_h < 11.9\}$ (RPCDM). Note that the spin transition zone of the RPCDM model is located in the mass section below

$10^{12} h^{-1} M_\odot$. In other words, the halos with masses equal to or higher than $10^{12} h^{-1} \text{ Mpc}$ do not show a spin transition at $z = 0.4$ in the RPCDM model. The ΛCDM model can still be distinguished from the $w\text{CDM}$ model at $z = 0.4$ by the nonoverlapped m_h -interval of $12.1 \leq m_h < 12.2$, where the confidence level for the rejection of the null hypothesis drops below (stays above) 99.9% for the $w\text{CDM}$ (ΛCDM) case.

2.3. Dependence on the Web Type

To investigate how the spin transition zone of each model varies with the web type, we classify the halo environments into the four web types, namely, knots, filaments, sheets, and voids according to the signs of the tidal eigenvalues, $\{\lambda_i\}_{i=1}^3$ at the grids where each galactic halo is placed (Hahn et al. 2007b). Figure 10 (Figure 11) plots the same as Figure 1 (Figure 5) but using only those halos embedded in the filaments satisfying the condition of $\lambda_1 \geq \lambda_2 > 0$ and $\lambda_3 < 0$. The spin transition zones of the filament halos are determined to be $\Delta m_t = \{m_h | 12.3 \leq m_h < 12.4\}$ (ΛCDM), $\Delta m_t = \{m_h | 12.4 \leq m_h < 12.5\}$ ($w\text{CDM}$), and $\Delta m_t = \{m_h | 12.1 \leq m_h < 12.2\}$ (RPCDM). Comparing Figure 11 with Figure 5, we note that the spin transitions of the filament halos occur in relatively narrow mass intervals for all of the three models and that in the filaments the spin transition zones between the ΛCDM and the $w\text{CDM}$ cases are no longer overlapped, which explains why the

Figure 6. Same as Figure 1 but for the case of $R_f = 5 h^{-1} \text{ Mpc}$.Figure 7. Same as Figure 5 but for the case of $R_f = 5 h^{-1} \text{ Mpc}$.

Figure 8. Same as Figure 1 but at $z = 0.4$.Figure 9. Same as Figure 5 but at $z = 0.4$.

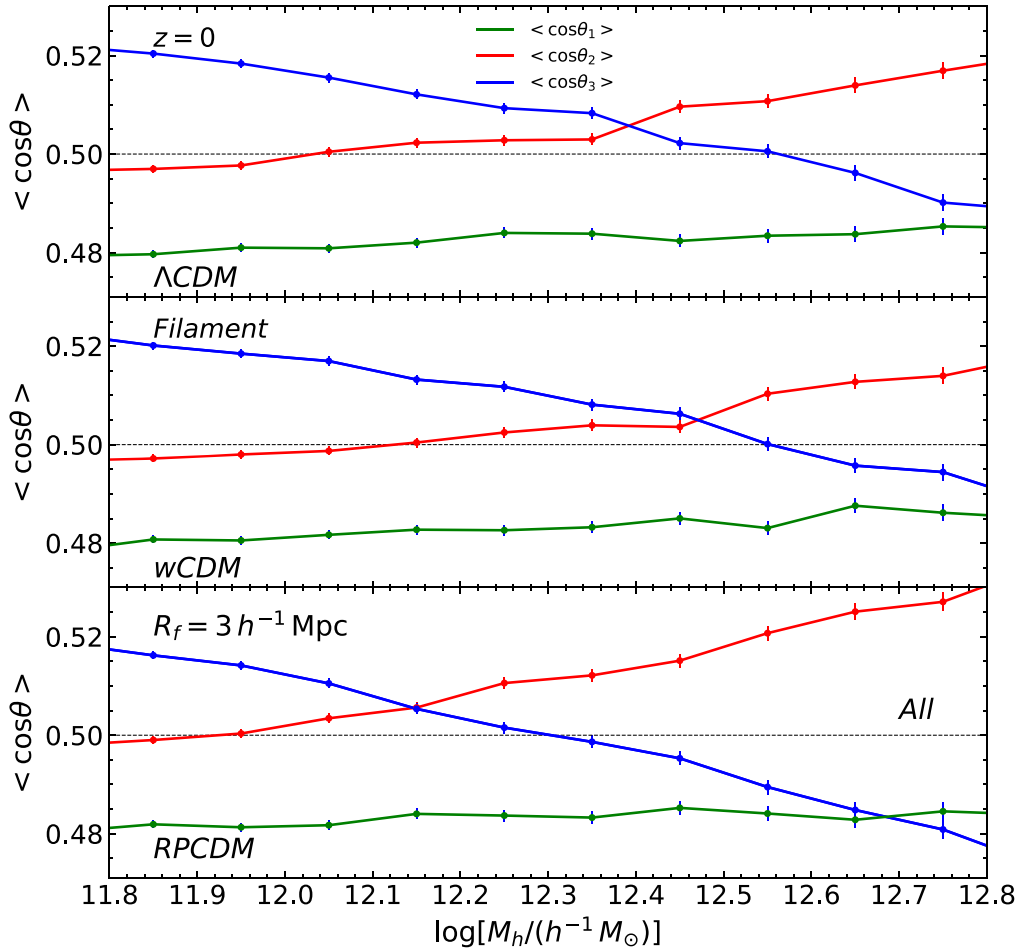


Figure 10. Same as Figure 1 but only with the filament halos.

filaments are the most optimal environments for the study of the halo spin transitions.

Figure 12 (Figure 13) plots the same as Figures 1 (Figure 5) but using only those halos in the sheets satisfying the condition of $\lambda_1 > 0$ and $\lambda_2 < 0$. As can be seen, the sheet halos exhibit the spin transitions, too (Wang & Kang 2017). Their spin transition zones are, however, shifted to the lower mass sections compared with those of the filament halos for all of the three models: $\Delta m_t = \{m_h | 11.7 \leq m_h < 12.1\}$ (ΛCDM), $\Delta m_t = \{m_h | 11.6 \leq m_h < 12.2\}$ ($w\text{CDM}$), and $\Delta m_t = \{m_h | 11.5 \leq m_h < 11.8\}$ (RPCDM). Comparing Figure 13 with Figure 5, we also note that the spin transitions of the sheet halos occur in relatively broad mass intervals for all of the three models and that in the sheets the spin transition zones are overlapped not only between the ΛCDM and $w\text{CDM}$ cases but also between the RPCDM and $w\text{CDM}$ cases, which indicates that the sheets are not so optimal as the filaments for the investigation of Δm_t as a discriminator of DE models. It is, however, worth mentioning here that for the $w\text{CDM}$ and RPCDM cases the sheet halos exhibit the spin transitions in the mass range lower than $\log[M_h/(h^{-1} M_\odot)] < 11.8$ where the directions of the halo spin vectors are likely to be inaccurate due to the low particle resolution (Bett et al. 2007). For a more accurate investigation of the spin transition of the sheet halos, it will be necessary to use data from a higher-resolution N -body simulation.

We have also determined the spin transition zones of the halos embedded in the knots ($\lambda_3 > 0$) and voids ($\lambda_1 < 0$) for

each model and found that the three DE models cannot be discriminated from one another by the spin transition zones of the knot halos or by the void halos due to the large uncertainties. We leave out the results for the cases of the knot and void halos.

3. Discussion and Conclusion

In light of the recent finding of Lee et al. (2020) that the halo spin transitions can be a powerful probe of the total neutrino mass, we have investigated whether or not it can be also used to discriminate nonstandard DE models from the standard ΛCDM cosmology. For this investigation, we appropriated the halo catalogs from the DEUS, which were performed for different DE models, ΛCDM , $w\text{CDM}$ and RPCDM, which satisfy equally well the constraints from the WMAP7 and SN Ia observations (see Table 1) (Alimi et al. 2012). The probability density functions of the cosines of the angles between the halo spin axes and the intermediate (minor) principal axes of the local tidal fields, $p(\cos \theta_2)$ ($p(\cos \theta_3)$), have been numerically evaluated for each DE model. Adopting the new definition introduced by Lee et al. (2020), we have determined for each model a spin transition zone, Δm_t , as the halo mass range in which the confidence level for the rejection of the null hypothesis of $p(\cos \theta_2) \sim p(\cos \theta_3)$ by the KS test descends below 99.9%.

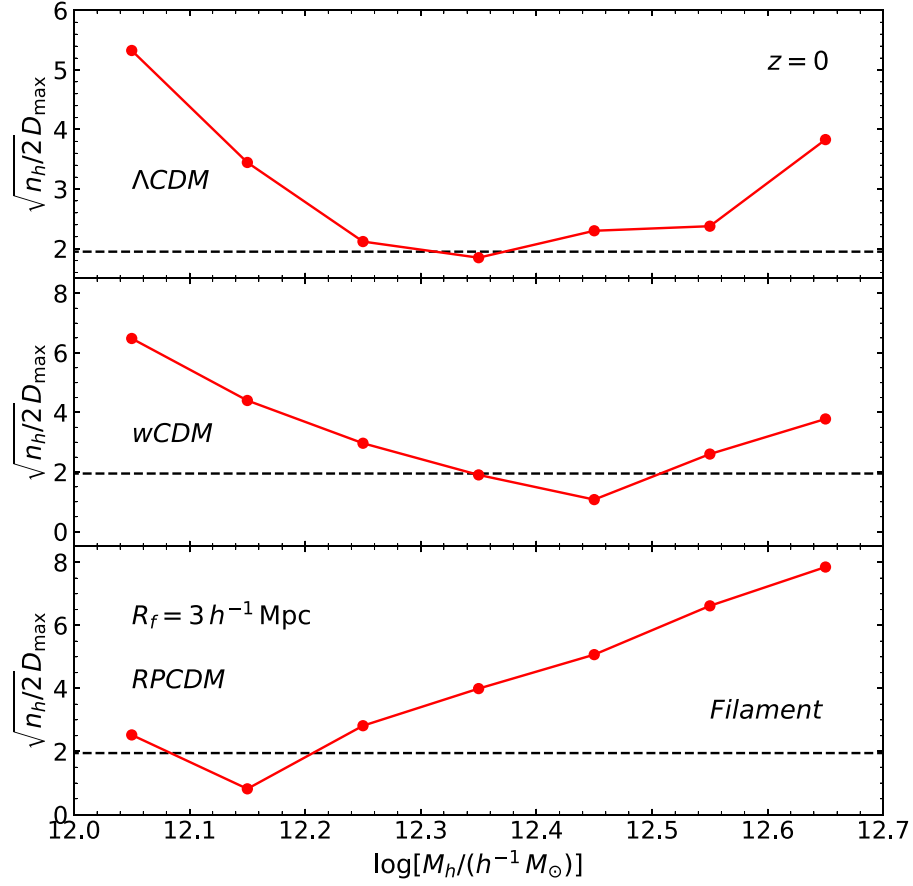


Figure 11. Same as Figure 5 but for the case of the filament halos.

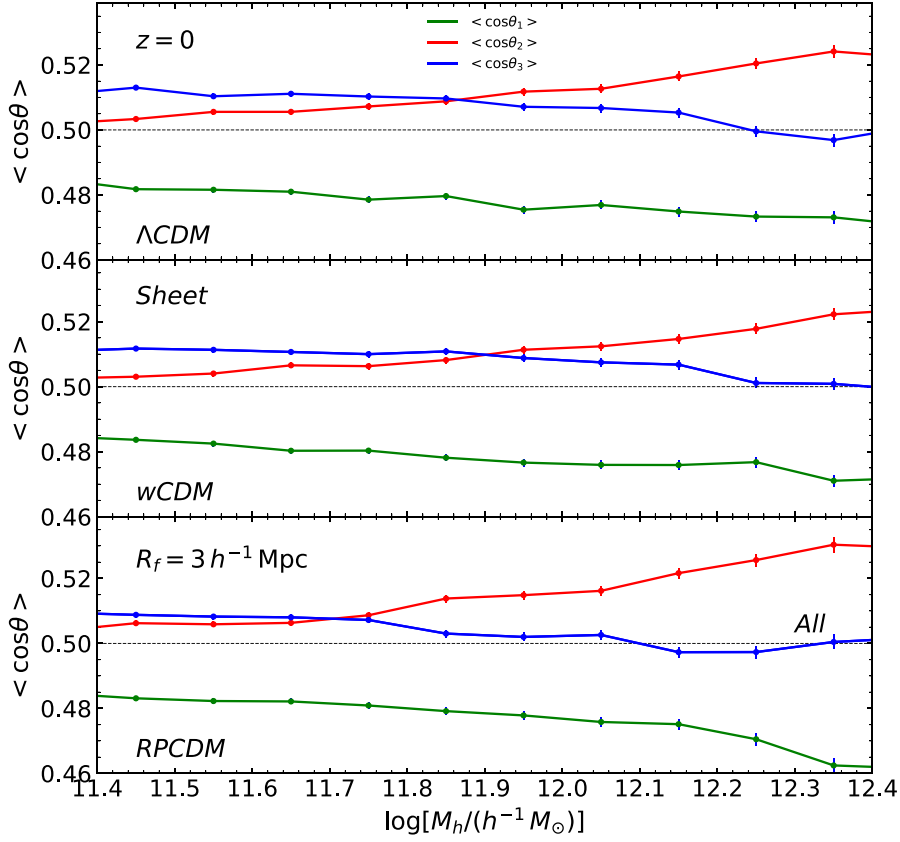


Figure 12. Same as Figure 1 but only with the sheet halos.

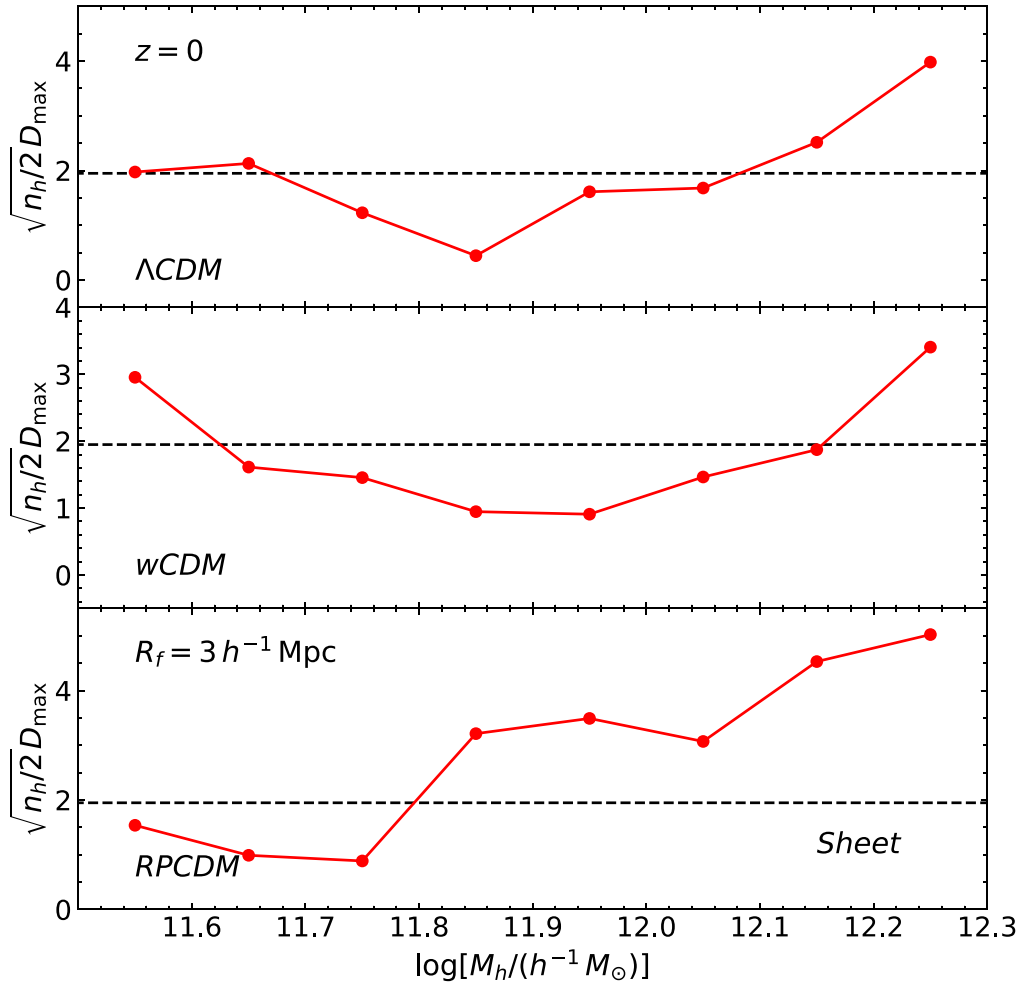


Figure 13. Same as Figure 5 but only with the sheet halos.

We have shown that the three DE models significantly differ in Δm_t among themselves. The summary of our results is the following (see also Table 2).

1. At $z = 0$, the spin transition zone of the RPCDM model resides in the lowest mass section among the three, which allows itself to be plainly distinguished from the Λ CDM model. Although the spin transition zone of the w CDM model is partially overlapped with that of Λ CDM, the w CDM model can still be discriminated with high statistical significance from the Λ CDM model by the largest halo mass contained in the spin transition zone at $z = 0$.
2. At higher redshifts $z = 0.4$, the overall strengths of the halo spin alignments with the tidal principal directions for all of the three models are enhanced, which leads the spin transition zone to be shifted toward the lower mass section, enlarging the differences in Δm_t among the three models.
3. The increase of the smoothing scale of the tidal fields undermines the alignment tendency of the halo spins with the tidal intermediate principal directions, shifting the spin transition zone toward the higher mass section for all of the three models. Nevertheless, the statistical significance of the differences in Δm_t among the three dark energy models is robust against the variations of the smoothing scales.

Table 2
Halo Spin Transition Zones

Model	Web Type	R_f (h^{-1} Mpc)	z	Δm_t
Λ CDM	all	3	0	[12.2, 12.4]
w CDM	all	3	0	[12.2, 12.5]
RPCDM	all	3	0	[12.0, 12.1]
Λ CDM	all	5	0	[12.3, 12.6]
w CDM	all	5	0	[12.3, 12.5]
RPCDM	all	5	0	[12.1, 12.3]
Λ CDM	all	3	0.4	[12.0, 12.1]
w CDM	all	3	0.4	[12.0, 12.2]
RPCDM	all	3	0.4	[11.8, 11.9]
Λ CDM	filament	3	0	[12.3, 12.4]
w CDM	filament	3	0	[12.4, 12.5]
RPCDM	filament	3	0	[12.1, 12.2]
Λ CDM	sheet	3	0	[11.7, 12.1]
w CDM	sheet	3	0	[11.6, 12.2]
RPCDM	sheet	3	0	[11.5, 11.8]

4. In the filaments, the strengths of the halo spin alignments with the tidal principal axes vary relatively rapidly with the halo mass, which leads the spin transition to occur in

a narrower mass range (i.e., narrower spin transition zone) for all of the three models. In consequence, the differences in the spin transition zone among the three models become more prominent in the filaments.

5. In the sheets, the strengths of the halo spin alignments with the tidal principal axes vary relatively slowly with the halo mass, which has an effect of widening the spin transition zone, shifting it to the lower mass section (see Wang & Kang 2017). In consequence, the differences in the spin transition zone among the three models become less prominent in the sheets.

Our results are in line with the claim of Lee et al. (2020) that the spin transition mass depends on how fast the nonlinear evolution of the tidal fields proceed. According to the linear tidal torque theory (White 1984), the spin axes of the galactic halos, \hat{S} , prefer the intermediate principal directions, \hat{p}_2 , of the linear tidal fields before the turn-around moments (Lee & Pen 2000, 2001). The subsequent nonlinear evolution of the tidal fields, however, gradually deviates their principal axes from the original directions, which lessens the linearly generated \hat{S} - \hat{p}_2 alignments and simultaneously promotes the \hat{S} - \hat{p}_3 alignments. According to this claim, the spin transition zone would shift toward the higher (lower) mass section in a model where the tidal field undergoes a faster (slower) nonlinear evolution. Given that the ratio of the linear growth factor in the Λ CDM (w CDM) model to that of the Λ CDM model is always below (above) unity (Alimi et al. 2012), the nonlinear evolution of the tidal field in the Λ CDM (w CDM) model is expected to proceed more slowly (rapidly) than that in the Λ CDM model, which explains why the spin transition in the former model occurs in the lower (higher) mass section than that of the latter model.

The bottom line is that the spin transition zone can in principle discriminate the nonstandard DE models from the standard Λ CDM model. The advantage of using the spin transition zone as a DE discriminator over the linear growth factor is that the spin transition zone can be estimated at the present epoch from real observational data, while the high- z data are required to estimate the linear growth factor. Moreover, recalling that the spin transition zone deals with more readily observable small-scale features of the universe, we speculate that it might contain additional information on the nonlinear evolution of structure formation, having a potential to break the other cosmic degeneracies. Our future work is in the direction of extending the current analysis to a broader range of nonstandard cosmologies and to more comprehensively study the efficacy of the halo spin transition zone as a probe of cosmology.

J.L. acknowledges the support of the Basic Science Research Program through the National Research Foundation (NRF) of Korea funded by the Ministry of Education (No. 2019R1A2C1083855) and also by a research grant from the NRF to the Center for Galaxy Evolution Research (No. 2017R1A5A1070354). N.I.L. acknowledges financial support of the Project IDEXLYON at the University of Lyon under the Investments for the Future Program (ANR-16-IDEX-0005). N.I.L. also acknowledges support from the joint Sino-German DFG research Project “The Cosmic Web and its impact on galaxy formation and alignment” (DFG-LI 2015/5-1).

ORCID iDs

Jounghun Lee  <https://orcid.org/0000-0003-0522-4356>

References

- Abbott, T. M. C., Abdalla, F. B., Alarcon, A., et al. 2018, *PhRvD*, **98**, 043526
- Agrawal, P., Cyr-Racine, F.-Y., Pinner, D., et al. 2019, arXiv:1904.01016
- Alimi, J.-M., Bouillot, V., Rasera, Y., et al. 2012, arXiv:1206.2838
- Alimi, J.-M., Füzfa, A., Boucher, V., et al. 2010, *MNRAS*, **401**, 775
- Aragón-Calvo, M. A., van de Weygaert, R., Jones, B. J. T., et al. 2007, *ApJL*, **655**, L5
- Aragón-Calvo, M. A., & Yang, L. F. 2014, *MNRAS*, **440**, L46
- Bett, P., Eke, V., Frenk, C. S., et al. 2007, *MNRAS*, **376**, 215
- Blue Bird, J., Davis, J., Luber, N., et al. 2019, arXiv:1912.01062
- Bouillot, V. R., Alimi, J.-M., Corasaniti, P.-S., et al. 2015, *MNRAS*, **450**, 145
- Caldwell, R. R., Kamionkowski, M., & Weinberg, N. N. 2003, *PhRvL*, **91**, 071301
- Carroll, S. M. 2001, *LRR*, **4**, 1
- Carroll, S. M. 2006, *Natur*, **440**, 1132
- Codis, S., Gavazzi, R., Dubois, Y., et al. 2015a, *MNRAS*, **448**, 3391
- Codis, S., Jindal, A., Chisari, N. E., et al. 2018, *MNRAS*, **481**, 4753
- Codis, S., Pichon, C., Devriendt, J., et al. 2012, *MNRAS*, **427**, 3320
- Codis, S., Pichon, C., & Pogosyan, D. 2015b, *MNRAS*, **452**, 3369
- Dubois, Y., Pichon, C., Welker, C., et al. 2014, *MNRAS*, **444**, 1453
- Forero-Romero, J. E., Contreras, S., & Padilla, N. 2014, *MNRAS*, **443**, 1090
- Ganeshaiah Veena, P., Cautun, M., Tempel, E., et al. 2019, *MNRAS*, **487**, 1607
- Ganeshaiah Veena, P., Cautun, M., van de Weygaert, R., et al. 2018, *MNRAS*, **481**, 414
- Hahn, O., Carollo, C. M., Porciani, C., et al. 2007a, *MNRAS*, **381**, 41
- Hahn, O., Porciani, C., Carollo, C. M., et al. 2007b, *MNRAS*, **375**, 489
- Hahn, O., Teyssier, R., & Carollo, C. M. 2010, *MNRAS*, **405**, 274
- Hikage, C., Oguri, M., Hamana, T., et al. 2019, *PASJ*, **71**, 43
- Hirv, A., Pelt, J., Saar, E., et al. 2017, *A&A*, **599**, A31
- Komatsu, E., Smith, K. M., Dunkley, J., et al. 2011, *ApJS*, **192**, 18
- Kraljic, K., Davé, R., & Pichon, C. 2020, *MNRAS*, **493**, 362
- Kreisch, C. D., Cyr-Racine, F.-Y., & Doré, O. 2020, *PhRvD*, **101**, 123505
- Krolewski, A., Ho, S., Chen, Y.-C., et al. 2019, *ApJ*, **876**, 52
- Laigle, C., Pichon, C., Codis, S., et al. 2015, *MNRAS*, **446**, 2744
- Lee, J. 2019, *ApJ*, **872**, 37
- Lee, J., Libeskind, N. I., & Ryu, S. 2020, *ApJ*, **898**, 27
- Lee, J., & Pen, U.-L. 2000, *ApJL*, **532**, L5
- Lee, J., & Pen, U.-L. 2001, *ApJ*, **555**, 106
- Libeskind, N. I., Hoffman, Y., Forero-Romero, J., et al. 2013, *MNRAS*, **428**, 2489
- Linder, E. V. 2003, *PhRvL*, **90**, 091301
- Pahwa, I., Libeskind, N. I., Tempel, E., et al. 2016, *MNRAS*, **457**, 695
- Paz, D. J., Stasyszyn, F., & Padilla, N. D. 2008, *MNRAS*, **389**, 1127
- Perlmutter, S., Aldering, G., Goldhaber, G., et al. 1999, *ApJ*, **517**, 565
- Planck Collaboration, Aghanim, N., Akrami, Y., et al. 2020, *A&A*, **641**, 6
- Poulin, V., Smith, T. L., Karwal, T., et al. 2019, *PhRvL*, **122**, 221301
- Rasera, Y., Alimi, J.-M., Courtin, J., et al. 2010, in AIP Conf. Proc. 1241, Invisible Universe (Melville, NY: AIP), 1134
- Ratra, B., & Peebles, P. J. E. 1988, *PhRvD*, **37**, 3406
- Riess, A. G., Casertano, S., Yuan, W., et al. 2019, *ApJ*, **876**, 85
- Riess, A. G., Filippenko, A. V., Challis, P., et al. 1998, *AJ*, **116**, 1009
- Roy, F., Bouillot, V. R., & Rasera, Y. 2014, *A&A*, **564**, A13
- Spergel, D. N., Bean, R., Doré, O., et al. 2007, *ApJS*, **170**, 377
- Springel, V., Frenk, C. S., & White, S. D. M. 2006, *Natur*, **440**, 1137
- Tegmark, M., Blanton, M. R., Strauss, M. A., et al. 2004, *ApJ*, **606**, 702
- Tempel, E., & Libeskind, N. I. 2013, *ApJL*, **775**, L42
- Tempel, E., Stoica, R. S., & Saar, E. 2013, *MNRAS*, **428**, 1827
- Trowland, H. E., Lewis, G. F., & Bland-Hawthorn, J. 2013, *ApJ*, **762**, 72
- Wang, P., Guo, Q., Kang, X., et al. 2018, *ApJ*, **866**, 138
- Wang, P., & Kang, X. 2017, *MNRAS*, **468**, L123
- Wang, P., & Kang, X. 2018, *MNRAS*, **473**, 1562
- Welker, C., Bland-Hawthorn, J., Van de Sande, J., et al. 2020, *MNRAS*, **491**, 2864
- Welker, C., Devriendt, J., Dubois, Y., et al. 2014, *MNRAS*, **445**, L46
- White, S. D. M. 1984, *ApJ*, **286**, 38